Supporting Information

High-Efficiency and Durable Inverted Perovskite Solar Cells with Thermally-Induced Phase-Change Electron Extraction Layer

Xin Li[1,4], Yun Meng[2], Ruizhe Liu[3], Zhiyao Yang[3], Yan Zeng[5], Yuanping Yi[5], Wei E.I. Sha[3]*, Yi Long[2,6,7]*, and Junyou Yang[1]**

1. State Key Laboratory of Material Processing and Die & Mould Technology, School of Materials Science and Engineering, Huazhong University of Science and Technology, Wuhan 430074, P. R. China.

2. School of Materials Science and Engineering, Nanyang Technological University, Singapore 639798, Singapore.

3. State Key Laboratory of Modern Optical Instrumentation, College of Information Science and Electronic Engineering, Zhejiang University, Hangzhou 310027, P. R. China.

4. Solar Energy Research Institute of Singapore, National University of Singapore, Singapore 117574, Singapore.

5. Beijing National Laboratory for Molecular Sciences, CAS Key Laboratory of Organic Solids, Beijing 100190, P. R. China

6. Singapore-HUJ Alliance for Research and Enterprise (SHARE), Campus for Research Excellence and Technological Enterprise (CREATE), Singapore 138602, Singapore

7. Sino-Singapore International Joint Research Institute (SSIJRI), Guangzhou 510000, P. R. China

*Corresponding author E-mail:

xin.li@nus.edu.sg; weisha@zju.edu.cn; longyi@ntu.edu.sg; jyyang@hust.edu.cn

Experimental Section

Materials. All the commercial materials were used as received. Lead iodide (PbI_2) and lead bromide ($PbBr_2$) was purchased from TCI. *N, N*-dimethylformamide (DMF), dimethylsulfoxide (DMSO), chlorobenzene (CB), toluene, and isopropanol (IPA) were purchased from Sigma-Aldrich. Formamidinium iodide (FAI) and methylammonium bromide (MABr) were purchased from GreatCell Solar (Australia). Phenyl-C61-butyric acid methyl ester ($PC_{61}BM$), poly[bis(4-phenyl) (2,4,6-trimethylphenyl) amine] (PTAA), cesium iodide (CsI), and bathocuproine (BCP) were purchased from Xi'an Polymer Light Technology Co., Ltd. Vanadium dioxide (VO_2) nanoparticles were directly purchased from Jingcheng Chemicals Co., Ltd, China or were prepared according to other published work. ITO-coated glasses were purchased from Yingkou You Xuan Trade Co., Ltd. Other chemicals were purchased from Aladdin.

VO_2 dispersed solution. The 25 mg VO_2 nanoparticles were first dispersed in 5 ml ethanol. In order to obtain continuous VO_2 films, the dispersant (that is Si-Al gel), was mixed with VO_2 in ethanol with volume ratio of 1: 1. The preparation method of Si-Al gel was reported by us previously *[J. Colloid. Interface. Sci., 2014, 427:*

49-53]. The as-prepared VO_2 solution was then stirred for 2 h and stored for use without further processing.

Device Fabrication. The ITO glass substrates were sequentially cleaned by ultrasonication with detergent, deionized water, acetone and IPA for 15 min, respectively. The cleaned ITO substrates were transferred into an oven at 100°C for drying and treated with O_2 plasma for 15 min before use. Then, the hole transport layer, that is 10 mg ml^{-1} PTAA in toluene, was spin-coated onto the ITO glass substrate at 4000 rpm for 30 s and this was subsequently annealed at 150°C for 10 min. For the fabrication of perovskite films, a typical one-step anti-solvent deposition method was obtained in this work. 1.4 M perovskite precursor solutions were prepared by mixing FAI, PbI_2, MABr, $PbBr_2$ and CsI in DMF: DMSO mixed solvent (4:1/v:v) with a chemical formula of $Cs_{0.05}(FA_{0.92}MA_{0.08})_{0.95}Pb(I_{0.92}Br_{0.08})_3$. The perovskite precursor solution was spin-coated at 2000 rpm for 10 s and 4000 rpm for 50 s onto the PTAA coated ITO substrate, 150 μL CB as anti-solvent was dripped on the film at 10 s before the end of the last procedure and then annealed at 100°C for 30 min. Subsequently, the devices were successively spin-coated with $PC_{61}BM$ (20 mg ml^{-1} in CB) at the rate of 1500 rpm for 45 s, annealed at 90°C for 10 min. An ultra-thin (5 nm) BCP was

deposited on the $PC_{61}BM$ surface by thermal evaporation to form a remarkable Ohmic contact to suppress the charge accumulation at the interface of ETL/metal electrodes. For the electron extraction layer, the VO_2 as-dispersed solution was spin-coated on the above $PC_{61}BM$ electron transport layer at different spin rate. Finally, 100 nm thick Ag was thermally evaporated on top through a shadow mask. The device active area was measured to 0.12 cm^2.

Computational Methods. Density function theory (DFT) calculations were performed using the Vienna Ab initio Simulation Package (VASP 5.4.1) *[1. J. Comput. Chem., 2008, 29, 2044– 2078]*. The projector augmented wave (PAW) method with the Perdew−Burke−Ernzerhof (PBE) exchange-correlation functional was used *[2. Phys. Rev. B, 1994, 50 (24), 17953-17979; 3. Phys. Rev. Lett., 1996, 77, 3865–3868]*. Plane-wave cutoff energy of 400 eV and energy convergence criterion of 10-8 eV was adopted for the self-consistent cycle throughout calculations. During the structural relaxation, 5×6×5 and 6×6×9 Monkhorst-Pack k-point meshes were employed for monoclinic VO_2 and rutile VO_2, respectively. For accurate calculations of the electronic properties, we adopted the DFT+U at the same theory level with a more dense k-mesh of 10×11×10 and 11×11×18 for the monoclinic VO_2 and rutile VO_2,

respectively. The Coulomb interaction parameter (U) and exchange interaction parameter (J) for the 3d atomic orbital of V were set to 2.8 and 0.93 eV, respectively *[4. Phys. Rev. Lett., 1999, 83(20), 4136-4139]*.

Characterization. The surface morphologies and microstructures of the pervoskite and VO_2 films and the cross-sectional of perovskite devices were investigated by a field emission scanning electron microscopy (SEM, GeminiSEM300, Carl Zeiss) equipped with an energy-dispersive X-ray spectrometer (EDS). The VO_2 films were scraped, dispersed in ethanol, and then observed by transmission electron microscopy (TEM, JEM-2100, JEOL Ltd). X-ray photoelectron spectroscopy (XPS) measurement was carried out by a AXIS-ULTRA DLD-600W surface-analysis system equipped with a monochromatic Al Kα X-ray source (1486.6 eV). Ultraviolet photoelectron spectroscopy (UPS) was measured using the XPS equipment, under irradiation with a He discharge lamp having the emission energy of 21.22 eV. Temperature-dependent crystal phases were conducted under different temperatures ranging from 25 to 105 °C during heating process by using X-ray diffraction (XRD, D8 Advance, Bruker) with Cu Kα irradiation, λ=1.5406 Å. UV-vis-NIR absorption and transmission spectrum of VO_2 films were recorded

by the UV-vis-NIR spectrophotometry (Lambda 950, PerkinElmer), equipped with a 150 mm integrating spheres for signal collection. The spectrophotometries were integrated with an accessory containing a customized heating and cooling stage and a digital controller (PE120, Linkam) for temperature-dependent measurement. Temperature dependent Raman spectrum analysis in the range of 100-1000 cm^{-1} wavenumber was done with a Renishaw inVia Raman microscope using 10% powered 514 nm laser. The work functions of the samples were investigated using ambient pressure photoemission spectroscopy with nitrogen environment (APS04-N2-RH, KP Technology Ltd). The steady-state photoluminescence (PL, excitation at 325 nm) and time-resolved photoluminescence (TRPL, excitation at 325 nm and emission at 760 nm) spectra were obtained using a lase spectrometer (FLS 980, Edinburgh Instruments Ltd). Electrochemical impedance spectroscopy (EIS) was measured by using a potentiostat (IviumStat 10800, Ivium Technologies) in a dark condition and a frequency range from 1MHz to 100 mHz. The transient photocurrent (TPC) decay and transient photovoltage (TPV) decay were recorded by electrochemical workstation (IviumStat 10800, Ivium Technologies) with a white light LED supplied 100 mW cm^{-2} light intensity to excite the perovskite solar cells. The current-voltage (*J-V*) characteristics of the devices were measured in

a nitrogen glove box by a Keithley 2400 Source Meter under standard AM 1.5G illumination with a xenon-lamp-base solar simulator (Enlitech, SS-F5-3A). For the temperature-dependent *J-V* curves, it were recorded from 25°C up to 85°C in steps of 10°C or 20°C under 1 Sun illumination. All temperature-dependent measurements were first taken in the N_2-glove box at room temperature (25°C), then to the highest temperature (85°C) and finally back at room temperature (25°C) and the devices were not encapsulated. Our *J-V* measurement system has been designed to be measured at different elevated temperature, which is integrated a small temperature-controlled heating table. So, the temperature can be tuned by the system software and this heating table. For contacting, a thermally coupled copper sample holder was used, placed on this temperature-controlled table and the thermocouple was attached the device's glass surface. Then device was in direct contact with the holder and reached the desired set temperature within a few minutes, as confirmed by the stabilized power output. Please note that the device should be waited about 10 mins for the MPP to stabilize the PCE output at the desired set temperature and then it can be measured for the *J-V* curves. During device heating between different temperatures, the device was always kept under 1 Sun illumination. Both forward scan (from -0.2 to 1.2 V) and reverse

scan (from 1.2 to -0.2 V) were performed with a delay time of 100 ms. An AR MgF_2 film is deposited on the incident side of ITO-coated glass substrate. The intensity of the light was calibrated with a KG-5 filter Si diode. The incident photon-to-electron conversion efficiency (IPCE) spectra were measured with a QE-R3011 IPCE system (Enli Technology Co., Ltd) ranging from 300 to 850 nm. The device thermal stability tests were also carried out in a nitrogen glove box, and the devices were put on a hotplate with a temperature of 85°C.

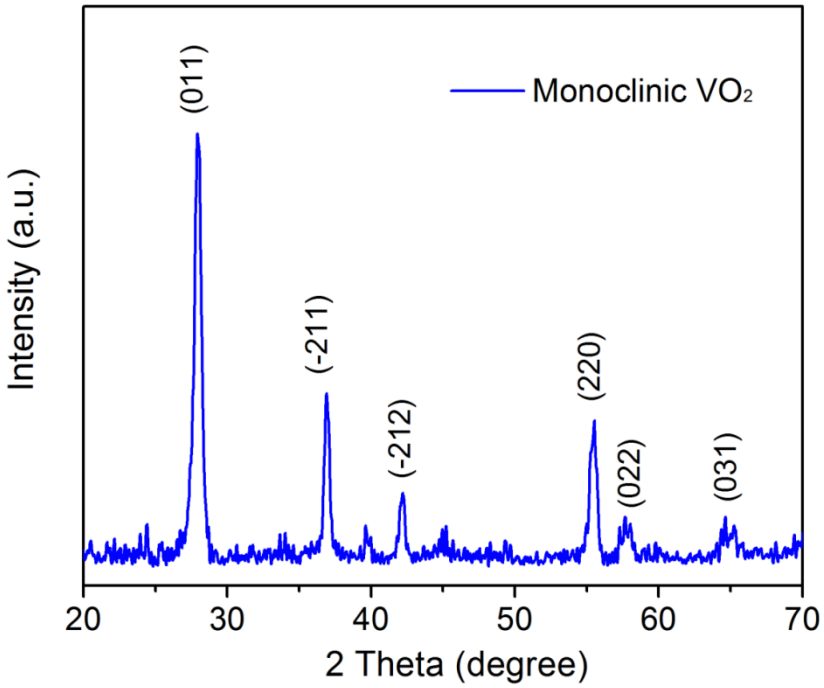

Figure S1. The XRD pattern of as-prepared VO_2 nanoparticles.

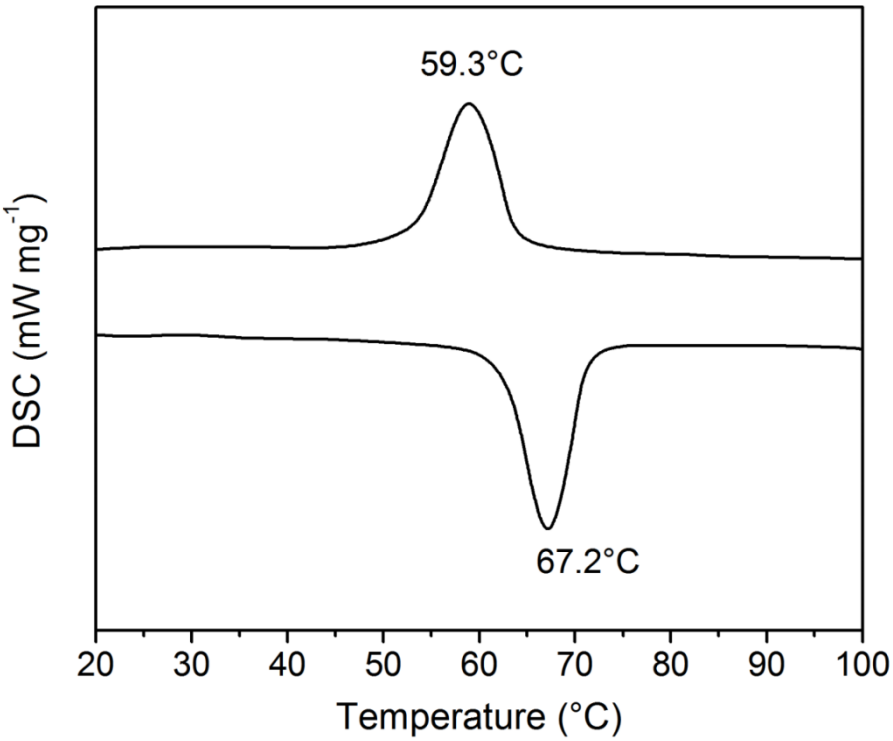

Figure S2. The DSC curves of the obtained VO_2 nanoparticles.

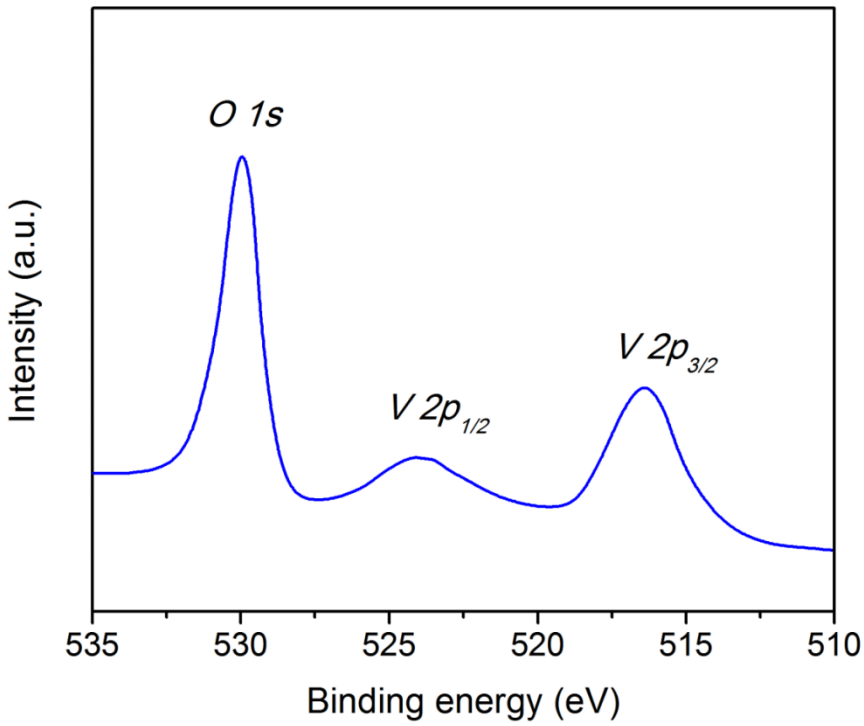

Figure S3. High-resolution XPS spectrum of as-prepared VO_2 film.

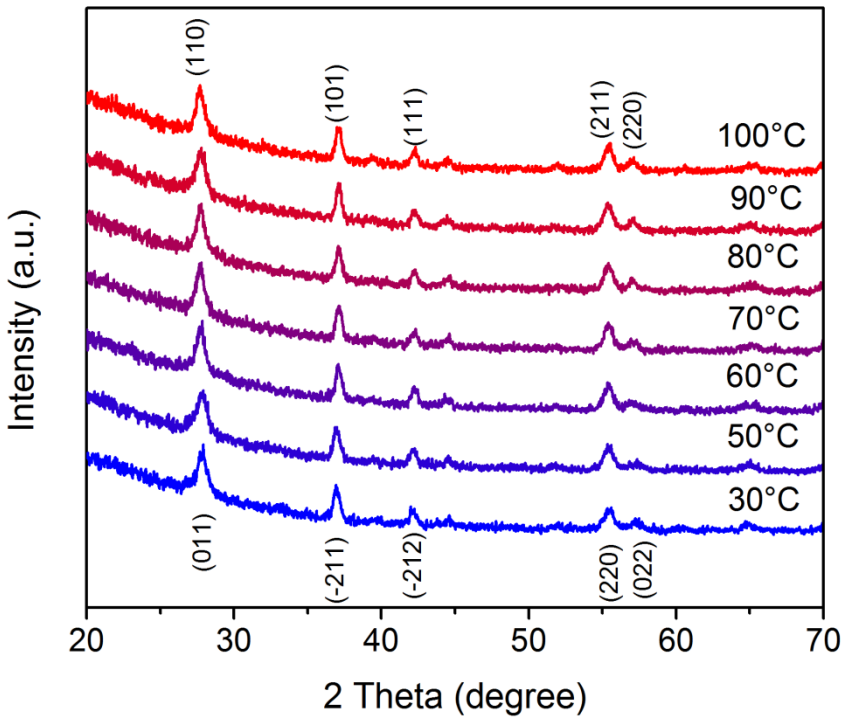

Figure S4. XRD patterns of VO_2 film (M/R) at temperature from 30 to 100°C. Note that the XRD pattern of VO_2 below 70°C has the same peak as shown in Figure S1.

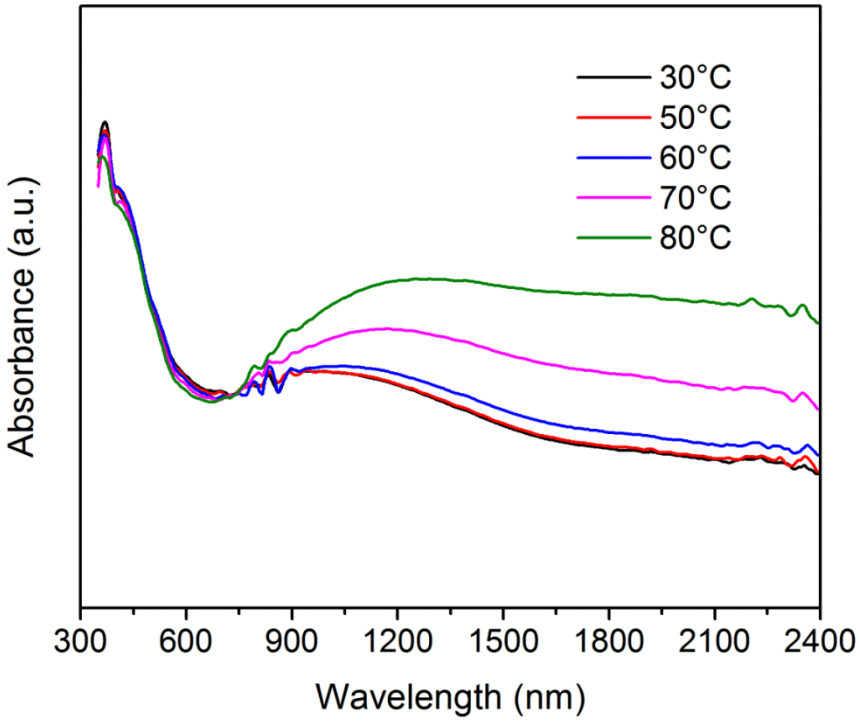

Figure S5. Temperature-dependent absorbance spectra of VO_2 film.

Figure S6. Photographs of the pure perovskite film (left) and the perovskite film covered by VO_2 layer (right) on PTAA-coated ITO substrates.

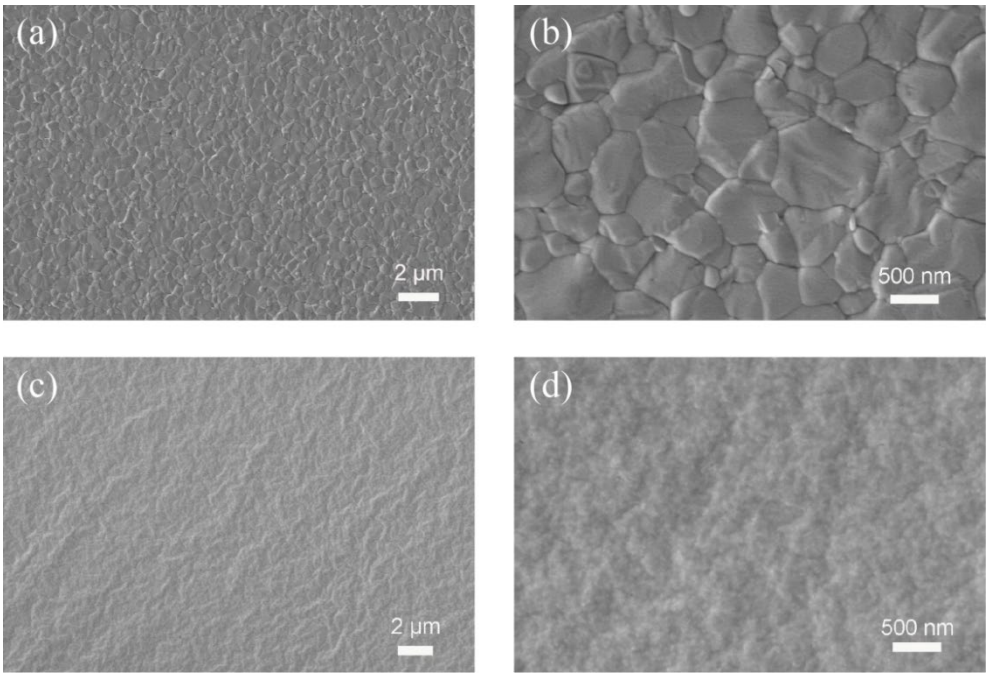

Figure S7. (a) SEM image of the perovskite film on the as-prepared PTAA/ITO substrate. (b) Corresponding magnified SEM image of the perovskite film on the PTAA/ITO substrate. (c) SEM image of as-deposited VO_2 film on the as-prepared perovskite/PTAA/ITO substrate. (d) Corresponding magnified SEM image of VO_2 film on the perovskite/PTAA/ITO substrate.

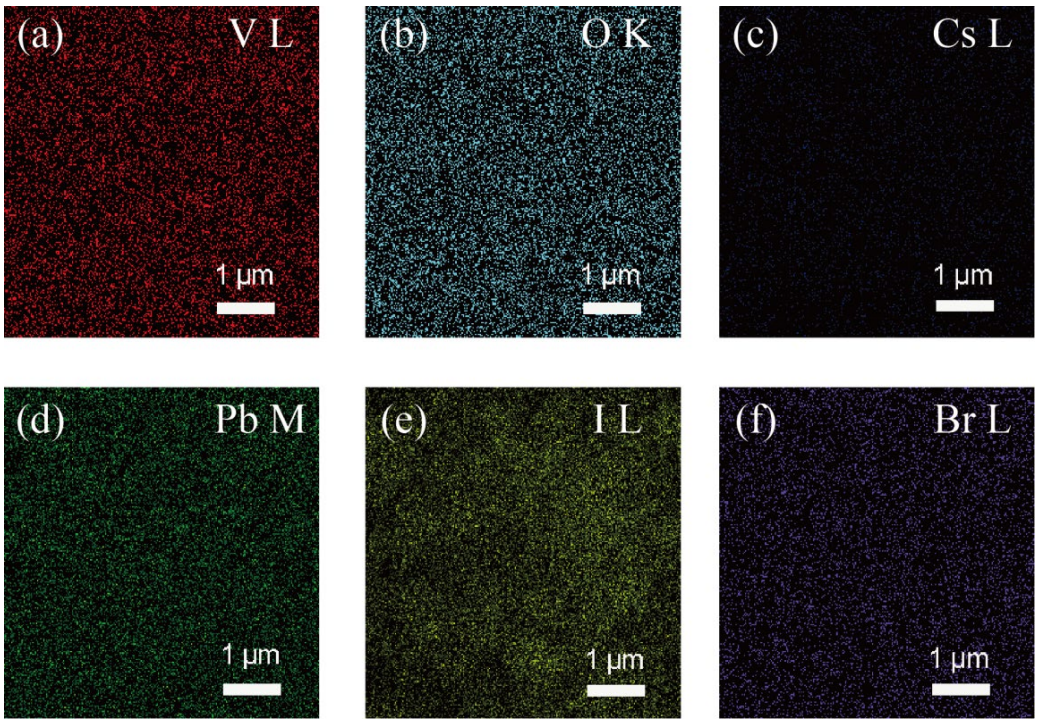

Figure S8. EDS mapping of V, O, Cs, Pb, I, and Br elements for the perovskite film covered by VO_2 layer, respectively.

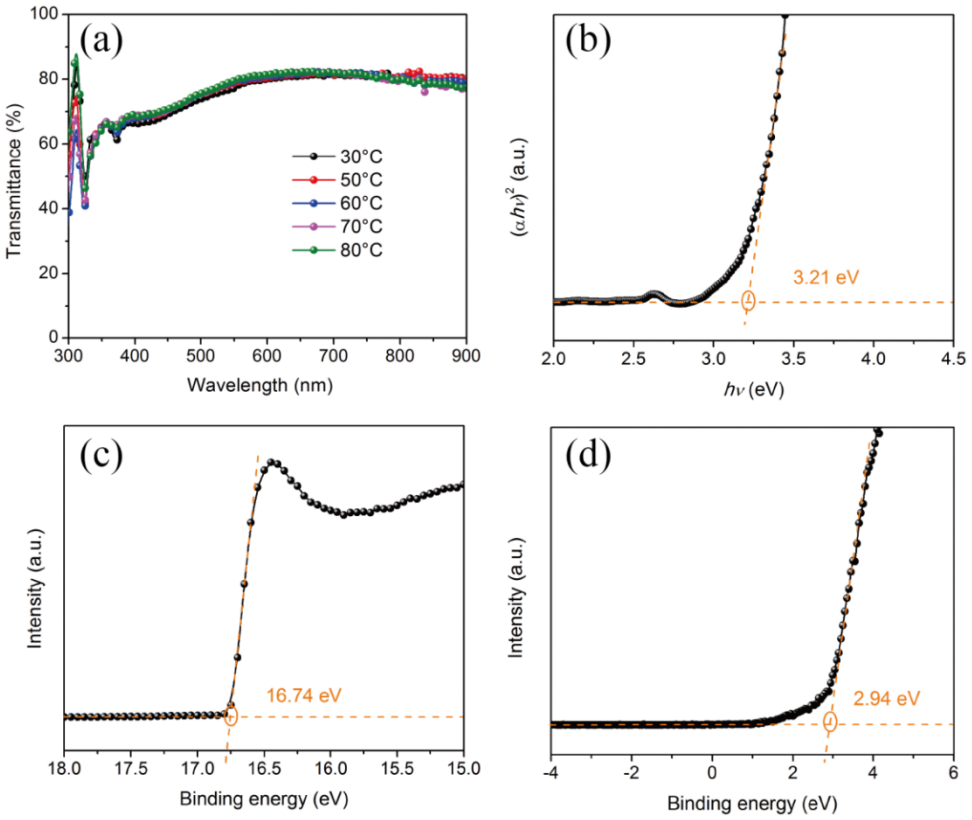

Figure S9. (a) Transmittance spectra of as-deposited VO_2 film on ITO substrate. (b) The extrapolated plots of $(\alpha hv)^2$ against hv obtained from the transmittance spectra of VO_2 film. The calculated optical bandgap of VO_2 is 3.21 eV. (c) The Fermi energy level of VO_2 obtained from UPS is 4.48 eV. (d) E_f - E_v of VO_2 is 2.94 eV. The calculated conduction band minimum for VO_2 is 4.21 eV.

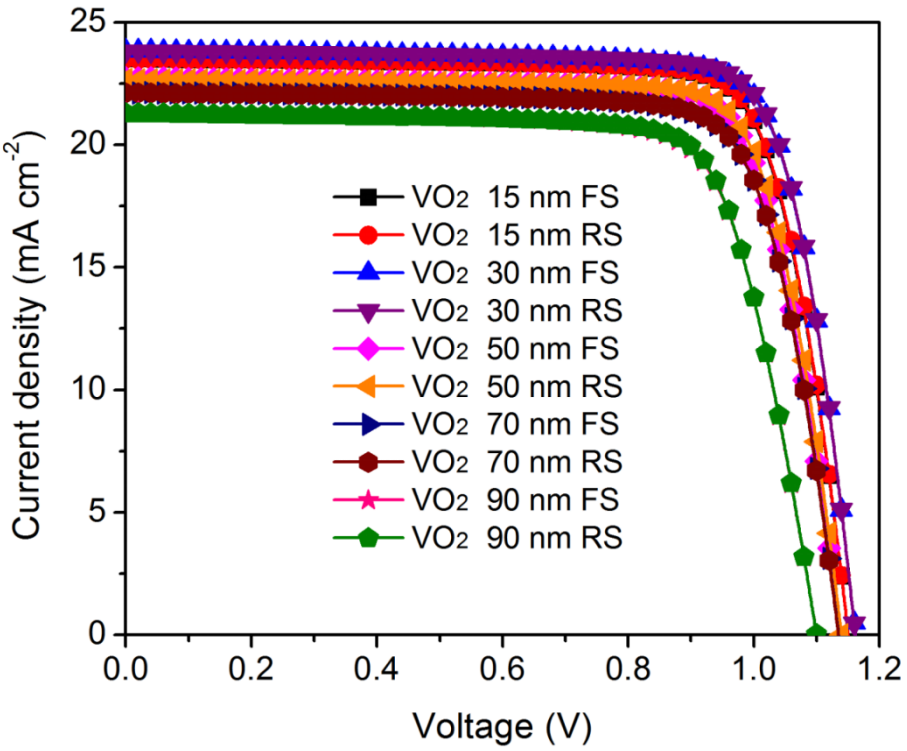

Figure S10. *J-V* curves of the devices based on different thicknesses of VO_2 layers under forward scan (FS) and reverse scan (RS).

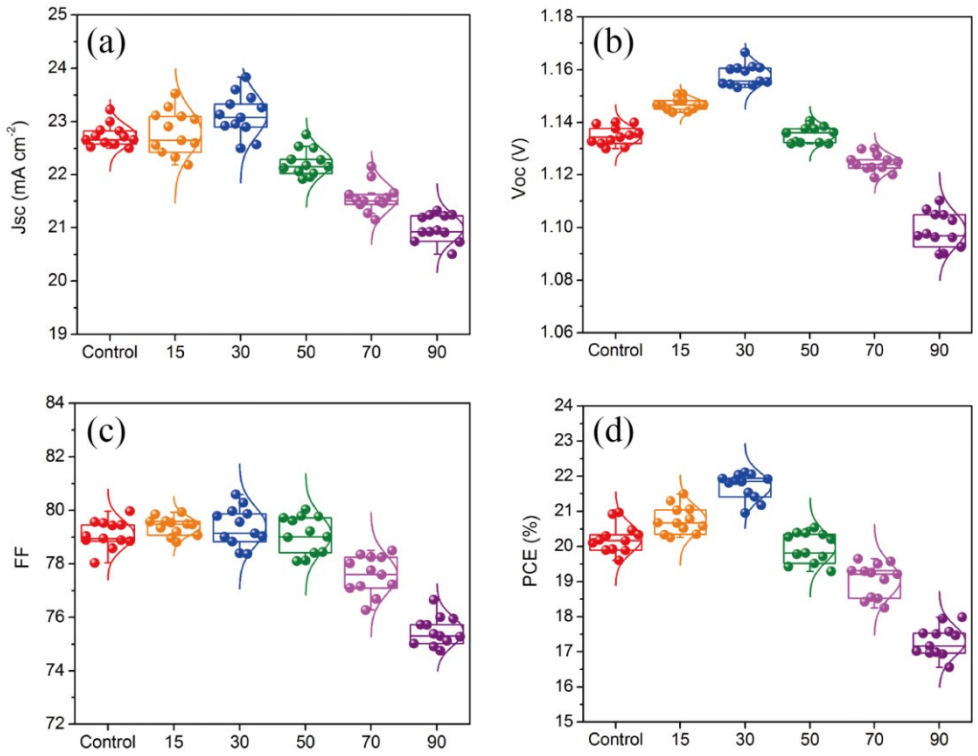

Figure S11. Box chart of photovoltaic parameters comparison of perovskite solar cells based on VO_2 with various thickness. The data were statistically analyzed from 12 cells per sample type (thickness). (a) J_{sc} (mA cm^{-2}), (b) V_{oc} (V), (c) *FF*, (d) PCE (%).

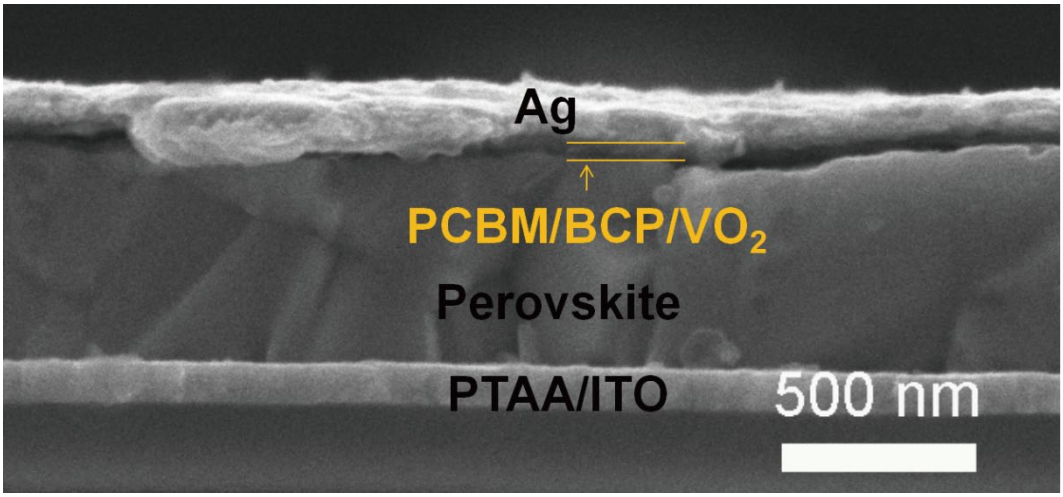

Figure S12. Cross-sectional SEM images of the studied device.

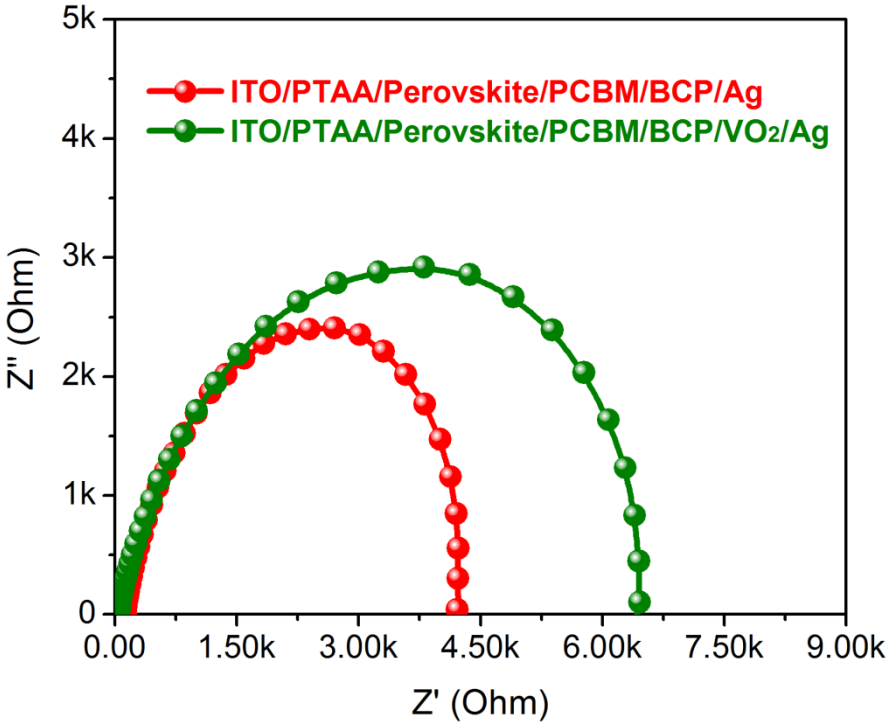

Figure S13. Nyquist plots of the EIS for the PSCs without and with VO_2 layer under dark condition at near open-circuit voltage.

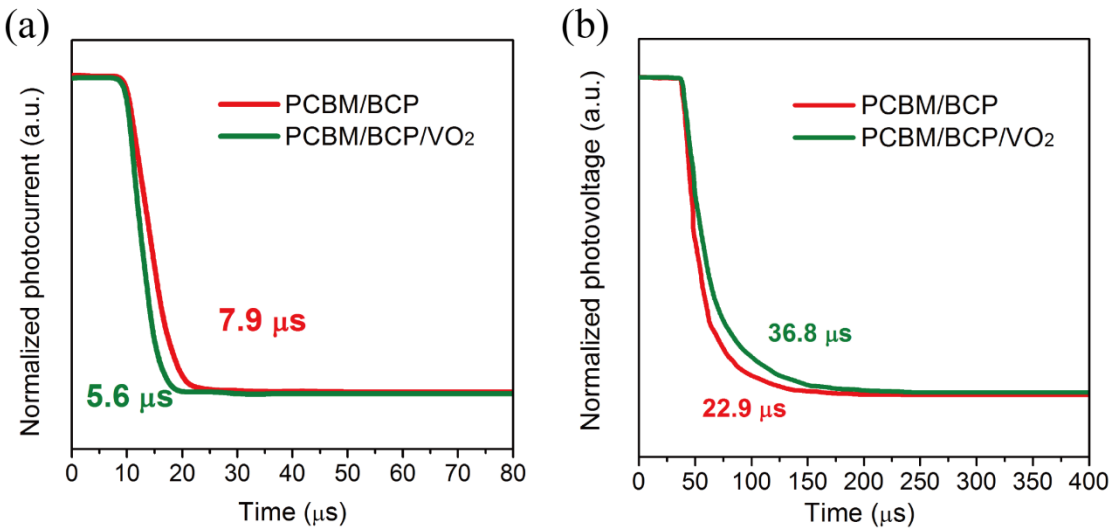

Figure S14. (a) Transient photocurrent (TPC) and (b) transient photovoltage (TPV) decay curves of PSCs.

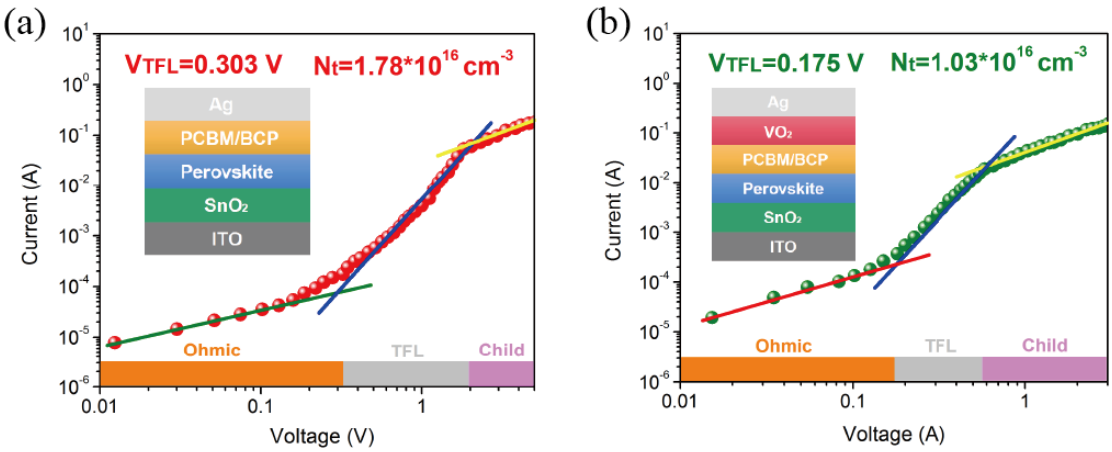

Figure S15. Light-intensity dependent (a) J_{sc} and (b) V_{oc} for the devices with or without VO_2 layer, respectively.

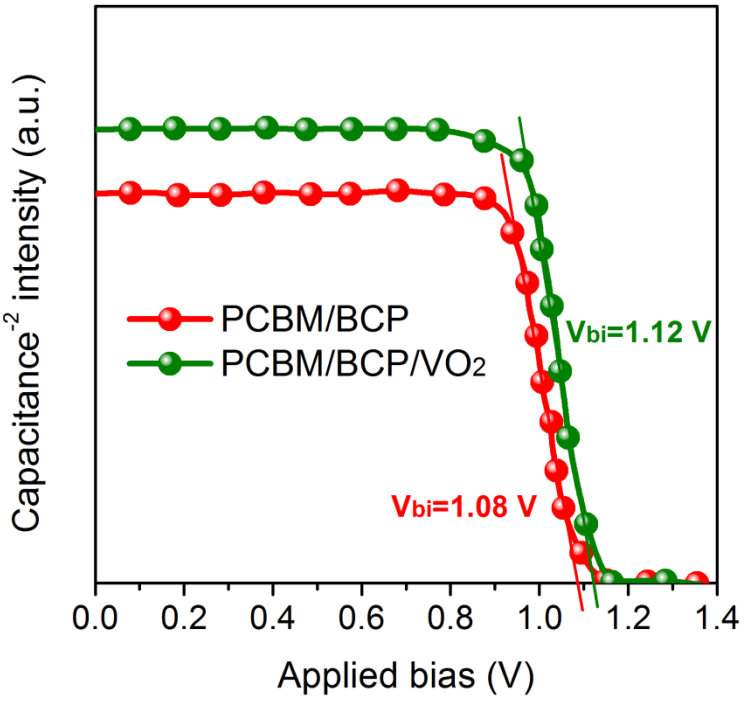

Figure S16. Mott-Schottky plots for the devices with and without VO_2 layer at 10 kHz.

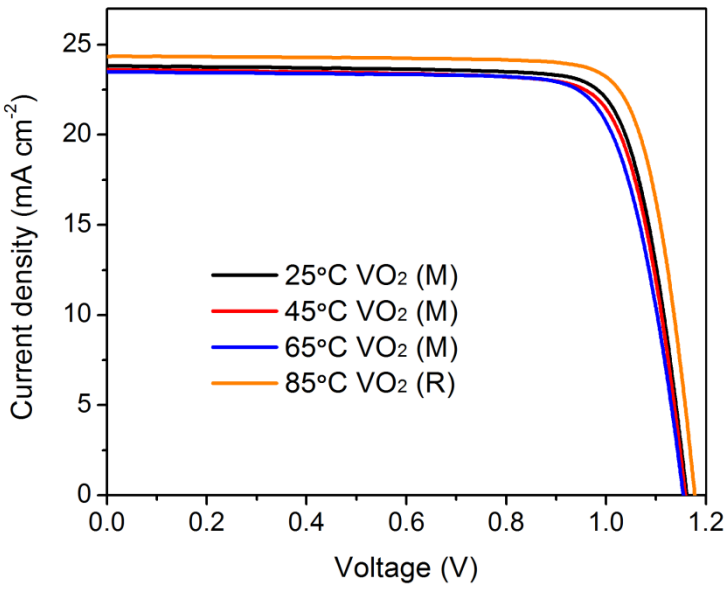

Figure S17. *J-V* curves of the VO_2-based device measured at 25°C, 45°C, 65°C, and 85°C, respectively.

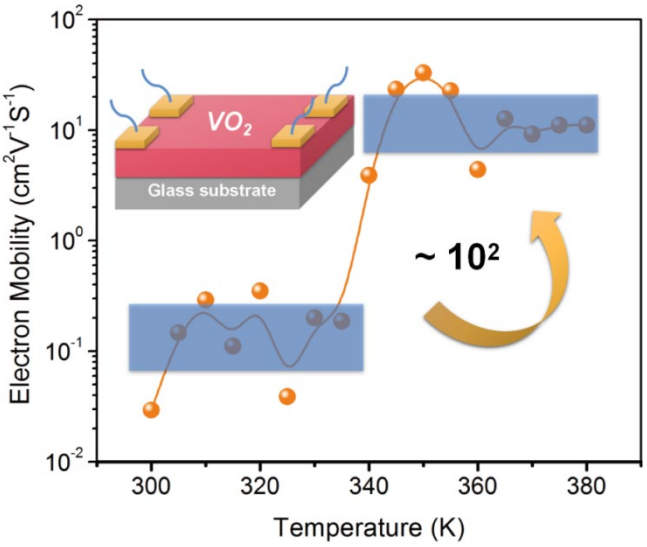

Figure S18. Temperature-dependent electron mobility of VO_2 film.

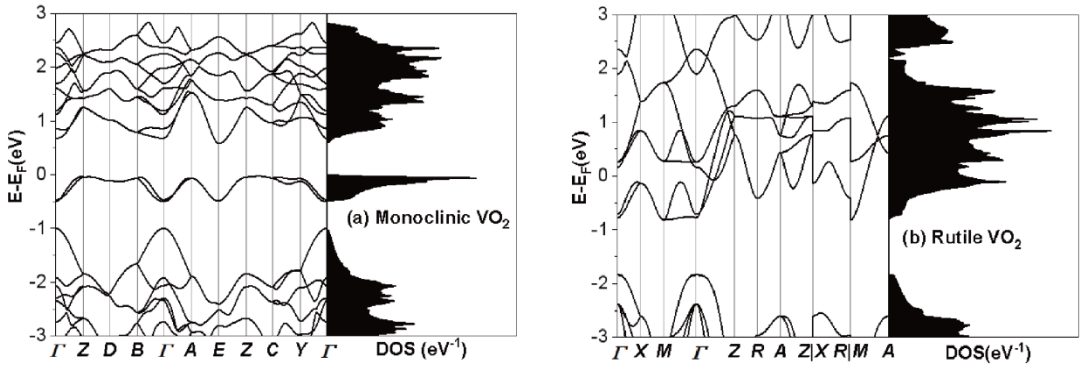

Figure S19. Band structures and density of states (DOS) of (a) Monoclinic VO_2, and (b) Rutile VO_2, respectively.

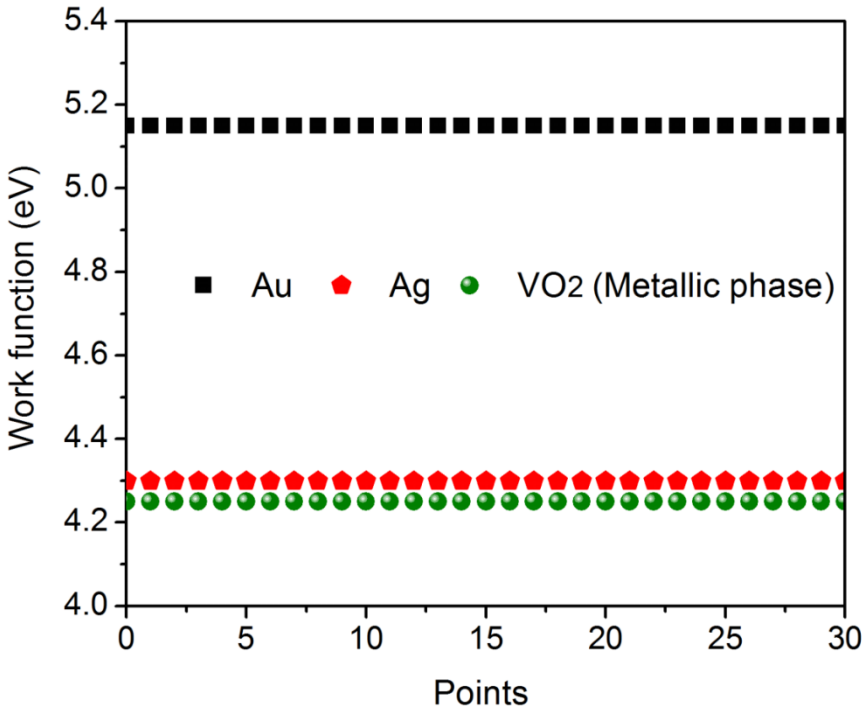

Figure S20. The work function of Au, Ag and VO_2 (metallic phase at 85°C). Before measuring, the WF of the tip was calibrated by a standard Au specimen with the WF of 5.15 eV.

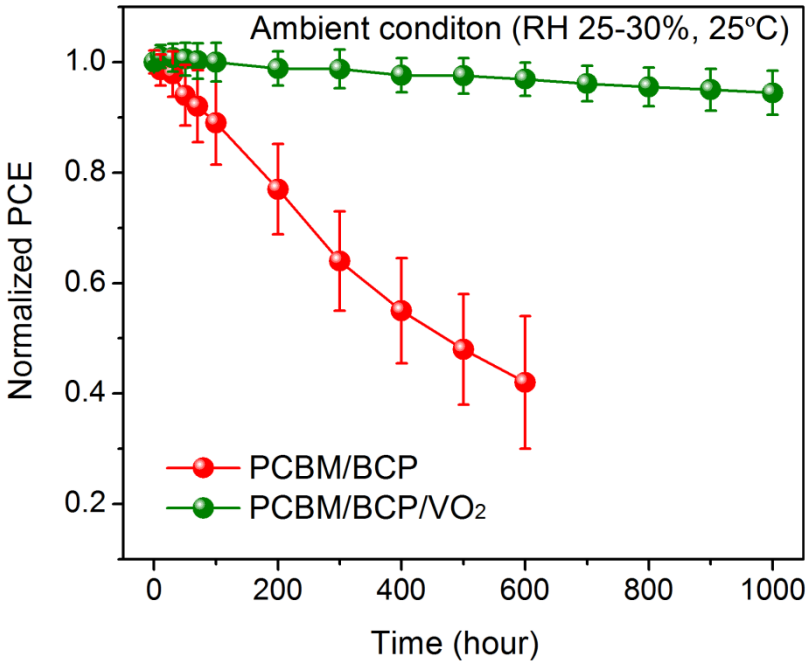

Figure S21. Long term device stability evaluation of the PSCs without and with VO_2 in dry box environment (RH 25-30%, 25°C) in the dark condition.

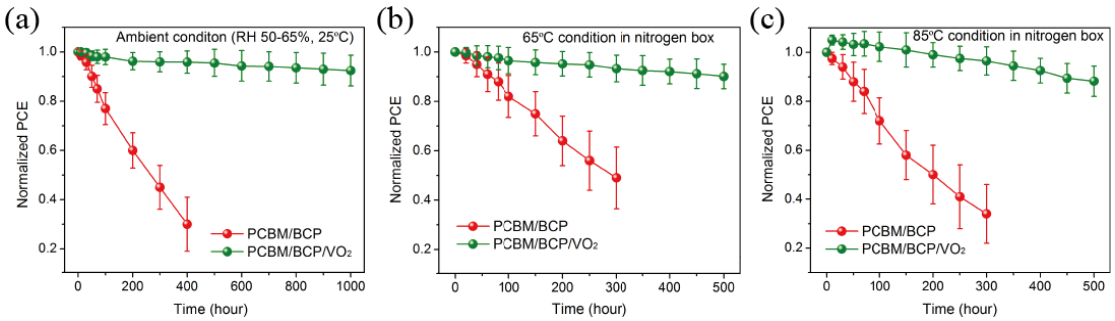

Figure S22. (a) Long-term stability of the devices with and without VO_2 layer under ambient condition (RH 50-65%, 25°C). (b) Thermal stability of the devices with and without VO_2 layer under 65°C in nitrogen box without any encapsulation. (c) Thermal stability of the devices with and without VO_2 layer under 85°C in nitrogen box without any encapsulation.

Table S1. Summary of the photovoltaic parameters based on devices with different thicknesses of VO_2 layers forward scan (FS) and reverse scan (RS).

VO_2 Thickness	Scan Direction	V_{oc} (V)	J_{sc} (mA cm^{-2})	FF	PCE
Control	RS	1.14	23.15	79.43	20.96
	FS	1.14	23.22	78.57	20.80
15 nm	RS	1.15	23.50	79.54	21.49
	FS	1.15	23.52	79.20	21.42
30 nm	RS	1.16	23.82	80.03	22.11
	FS	1.16	23.83	79.71	22.03
50 nm	RS	1.14	22.68	79.43	20.53
	FS	1.14	22.75	78.57	20.37
70 nm	RS	1.13	22.13	78.01	19.50
	FS	1.13	22.14	77.80	19.46
90 nm	RS	1.10	21.29	76.60	17.93
	FS	1.10	21.32	76.03	17.83

Table S2. PL decay curves of perovskite films based on different ETLs well fitted by a bi-exponential decay kinetics equation:

$$PL=A_1\exp(-t/\tau_1)+A_2\exp(-t/\tau_2),\ \tau_{avg}=\tau_1\times(A_1/A_1+A_2)+\tau_2\times(A_2/A_1+A_2)$$

Sample name	A_1 (%)	τ_1 (ns)	A_2 (%)	τ_2 (ns)	τ_{avg}
Perovskite (Pero)	12.9	7.6	87.1	179.9	157.6
Pero/VO_2	19.8	13.8	80.2	54.5	46.4
Pero/PCBM	34.3	11.7	65.7	44.0	32.9
Pero/PCBM/VO_2	12.3	5.3	87.7	28.2	25.4

Table S3. Summary of the photovoltaic performance of the reported high-efficiency PSCs with inverted configuration.

Device (Ref.)	V_{oc} (V)	J_{sc} (mA cm^{-2})	FF	PCE	Strategy
1	1.18	22.50	81.7	21.7	Additive engineering
2	1.21	22.50	79.0	21.5	N side engineering
3	1.21	22.49	78.5	21.4	Passivation engineering
4	1.12	23.05	80.3	20.7	P side engineering
5	1.13	23.30	80.0	21.1	Additive engineering
6	1.14	23.70	78.0	21.0	Passivation engineering
7	1.15	22.69	78.5	20.4	Additive engineering
8	1.13	22.40	80.0	20.3	Additive engineering
9	1.09	23.60	78.6	20.2	Novel HTL materials
10	1.12	23.23	81.4	21.2	Novel HTL materials
11	1.20	22.58	81.3	22.0	Novel ETL materials
12	1.14	23.68	81.0	21.9	Single-Crystal PSC
13	1.21	22.59	81.6	22.3	Interface engineering
14	1.17	24.10	81.6	23.0	Additive engineering
15	1.17	24.92	80.2	23.4	Interface engineering
This work	1.18	24.38	81.0	23.1	Interface modification

Table S4. Summary of the photovoltaic parameters for VO_2-based PSC measured at 25°C, 45°C, 65°C, and 85°C, respectively.

Temperature (°C)	V_{oc} (V)	J_{sc} (mA cm^{-2})	FF	PCE
25	1.164	23.82	80.03	22.11
45	1.159	23.63	79.38	21.73
65	1.154	23.45	78.74	21.30
85	1.178	24.38	81.03	23.11

Table S5. Lattice parameters of VO_2 crystal phases.

	a (Å)	*b* (Å)	*c* (Å)	*α* (°)	*β* (°)	*γ* (°)	
VO_2 (M)	5.398	4.500	5.390	90	115.330	90	Exp.
	5.335	4.529	5.357	90	116.483	90	Cal.
VO_2 (R)	4.542	4.542	2.872	90	90	90	Exp.
	4.563	4.563	2.775	90	90	90	Cal.

References

1. Wu W Q, Yang Z, Rudd P N, et al. Bilateral alkylamine for suppressing charge recombination and improving stability in blade-coated perovskite solar cells. Science advances, 2019, 5(3): eaav8925.
2. Luo D, Yang W, Wang Z, et al. Enhanced photovoltage for inverted planar heterojunction perovskite solar cells. Science, 2018, 360(6396): 1442-1446.
3. Yang S, Dai J, Yu Z, et al. Tailoring passivation molecular structures for extremely small open-circuit voltage loss in perovskite solar cells. Journal of the American Chemical Society, 2019, 141(14): 5781-5787.

4. Liu X, Cheng Y, Liu C, et al. 20.7% highly reproducible inverted planar perovskite solar cells with enhanced fill factor and eliminated hysteresis. Energy & Environmental Science, 2019, 12(5): 1622-1633.
5. Zheng X, Deng Y, Chen B, et al. Dual functions of crystallization control and defect passivation enabled by sulfonic zwitterions for stable and efficient perovskite solar cells. Advanced Materials, 2018, 30(52): 1803428.
6. Zheng X, Chen B, Dai J, et al. Defect passivation in hybrid perovskite solar cells using quaternary ammonium halide anions and cations. Nature Energy, 2017, 2(7): 1-9.
7. Wu T, Wang Y, Li X, et al. Efficient defect passivation for perovskite solar cells by controlling the electron density distribution of donor-π-acceptor molecules. Advanced Energy Materials, 2019, 9(17): 1803766.
8. Yu J C, Badgujar S, Jung E D, et al. Highly efficient and stable inverted perovskite solar cell obtained via treatment by semiconducting chemical additive. Advanced Materials, 2019, 31(6): 1805554.
9. Yang D, Sano T, Yaguchi Y, et al. Achieving 20% efficiency for Low-temperature-processed inverted perovskite solar cells. Advanced Functional Materials, 2019, 29(12): 1807556.
10. Wang Y, Chen W, Wang L, et al. Dopant-free small-molecule hole-transporting material for inverted perovskite solar cells with efficiency exceeding 21%. Advanced Materials, 2019, 31(35): 1902781.
11. Wu S, Li Z, Li M Q, et al. 2D metal-organic framework for stable perovskite solar cells with minimized lead leakage. Nature Nanotechnology, 2020, 15(11): 934-940.
12. Alsalloum A Y, Turedi B, Zheng X, et al. Low-temperature crystallization enables 21.9% efficient single-crystal $MAPbI_3$ inverted perovskite solar cells. ACS Energy Letters, 2020, 5(2): 657-662.
13. Wu S, Zhang J, Li Z, et al. Modulation of defects and interfaces through alkylammonium interlayer for efficient inverted perovskite solar cells. Joule, 2020, 4(6): 1248-1262.
14. Zheng X, Hou Y, Bao C, et al. Managing grains and interfaces via ligand anchoring enables 22.3%-efficiency inverted perovskite solar cells. Nature Energy, 2020, 5(2): 131-140.
15. Li F, Deng X, Qi F, et al. Regulating surface termination for efficient inverted perovskite solar cells with greater than 23% efficiency. Journal of the American Chemical Society, 2020, 142(47): 20134-20142.